# A circular zone of attachment to the extracellular matrix acts as a guidance system for *Toxoplasma gondii* 3D motility

Rachel V. Stadler[1], Shane R. Nelson[2], David M. Warshaw[2], Gary E. Ward[1]*

[1] Department of Microbiology and Molecular Genetics, and
[2] Department of Molecular Physiology and Biophysics,
University of Vermont Larner College of Medicine, Burlington, Vermont, U.S.A. 05405

* Correspondence to: Gary.Ward@uvm.edu

**Abstract**

*Toxoplasma gondii* is a protozoan parasite that infects 30-40% of the world's population. Infections are typically subclinical but can be severe and, in some cases, life threatening. Central to the virulence of *T. gondii* is an unusual form of substrate-dependent motility that enables the parasite to invade cells of its host and to disseminate throughout the body. A hetero-oligomeric complex of proteins that functions in motility has been characterized, but how these proteins work together to drive forward motion of the parasite remains controversial. A key piece of information needed to understand the underlying mechanism(s) is the directionality of the forces that a moving parasite exerts on the external environment. The linear motor model of motility, which has dominated the field for the past two decades, predicts continuous anterior-to-posterior force generation along the length of the parasite. We show here using three-dimensional traction force mapping that the predominant forces exerted by a moving parasite are instead periodic and directed in towards the parasite at a fixed circular location within the extracellular matrix. These highly localized forces, which are generated by the parasite pulling on the matrix, create a visible constriction in the parasite's plasma membrane. We propose that the circular ring of inward-directed force corresponds to a circumferential attachment zone between the parasite and the matrix, through which the parasite propels itself to move forward. The combined data suggest a closer connection between the mechanisms underlying parasite motility and host cell invasion than previously recognized. In parasites lacking the major surface adhesin, TgMIC2, neither the inward-directed forces nor the constriction of the parasite membrane are observed. TgMIC2-deficient parasites remain capable of moving at speeds similar to wildtype but the mutant parasites move in a less directed fashion, suggesting that TgMIC2-mediated circumferential adhesion of the parasite to the extracellular matrix serves, in part, as a guidance system to maximize forward displacement during parasite motility.

## Introduction

Parasites of the phylum Apicomplexa cause pervasive human disease and are responsible for millions of deaths annually. *Toxoplasma gondii* is the most prevalent apicomplexan parasite, infecting 30-40% of the human population worldwide [1-3]. *T. gondii* infections are typically subclinical in immunocompetent individuals but may cause blindness [4, 5]. In immunocompromised individuals and the developing fetus, the disease can be life-threatening [3, 6, 7].

*T. gondii* is a single-cell protozoan, and acute disease is caused by the highly motile tachyzoite life-cycle stage. Like other apicomplexan parasites, the *T. gondii* tachyzoite uses a unique form of substrate-dependent motility to invade into and egress from cells of its host, to migrate across biological barriers, and to disseminate throughout the infected host. Motility is, therefore, central to the pathogenesis of toxoplasmosis [8-10]. The parasite can move at speeds of up to 3 μm/s without the cilia, flagella, or leading edge protrusions that drive the motility of other eukaryotic cells. Within a three-dimensional (3D) extracellular matrix, the parasite moves along a complex helical trajectory characterized by regular oscillations in velocity and changes in trajectory curvature and torsion [11].

Motility is driven, at least in part, by a complex of proteins known as the glideosome, which is anchored to the inner membrane complex at the parasite periphery (Figure 1A). In the "linear motor" model of motility, short actin filaments are bound through a bridging protein to the cytosolic tails of transmembrane adhesins, such as TgMIC2, and translocated towards the posterior end of the parasite via a class XIV myosin, TgMyoA [12-15]. If the extracellular domains of the transmembrane adhesins are attached to ligands on the substrate, the rearward translocation of actin results in forward movement of the parasite. Other apicomplexan parasites, including those that cause malaria (*Plasmodium spp.*) and cryptosporidiosis, express similar glideosome proteins, suggesting that the mechanism of motility is conserved [16].

Although abundant evidence supports the importance of TgMyoA and other components of the glideosome in motility [10, 14, 17-21], several recent observations have raised questions about whether these proteins generate force as described by the linear motor model [17, 22-26] and, if so, whether this is the only motility mechanism available to the parasite. For example: (a) parasites conditionally depleted of TgMyoA and other glideosome components show greatly reduced motility but are not completely immotile [17, 22, 25], and (b) the linear motor model predicts uniformly forward directed motion, but under some conditions parasites are seen to repeatedly switch the directionality of their movement [27-30].

Because parasite motility is essential for virulence, elucidation of the underlying mechanism(s) is of both fundamental cell biological interest and potential clinical relevance. One key piece of missing information needed for a full mechanistic understanding of motility is the directionality of the forces the

parasite exerts on the external environment as it moves along its 3D helical trajectory. The linear motor model predicts continuous anterior-to-posterior forces along the entire periphery of the moving parasite. We show here using 3D traction force mapping that the predominant forces exerted by the parasite are instead organized into a highly localized circumferential ring of inward-directed force at a fixed location within the matrix. These inward-directed forces create a visible constriction of the parasite's plasma membrane, reflecting a circular zone of tight attachment of the parasite to the matrix through which the parasite passes through as it progresses forward along its helical trajectory. In the absence of this circular attachment zone, the parasite is still able to move but this movement loses much of its directionality.

## Results

### Development of a quantitative 3D traction force mapping assay

As a first step towards visualizing the forces exerted by parasites moving in 3D, we used a bead displacement assay in the well-established Matrigel extracellular matrix model [11, 25, 31]. Fluorescent microspheres embedded within the Matrigel were pulled towards a moving parasite from nearby anterior, posterior, and lateral locations within the matrix, and these microspheres returned to their original positions after the parasite had passed (Figure 1B, Videos 1&2). These results demonstrate that the parasite does indeed exert a detectable force on the surrounding matrix. Unexpectedly, we also noted constrictions in the body of the fluorescent parasite as it moved (Figure 1B, Video 1). These constrictions were even more apparent by brightfield microscopy (Fig. 1C, Video 3). Each constriction formed at the apical end of the parasite and remained stationary relative to the matrix as the parasite moved through, reminiscent of the "moving junction" through which the parasite penetrates during host cell invasion (discussed further below).

To develop a more quantitative force mapping assay and explore the relationship between the constrictions and matrix deformation, we used Alexa-Fluor 647-conjugated fibrinogen [32] to generate a fluorescent 3D fibrin matrix (Suppl. Figure 1A). The use of a fluorescent matrix enabled mapping of matrix displacements at all spatial points in our imaged volume rather than at the limited number of discrete positions offered by fluorescent microspheres. Parasite motility in matrices generated using 2.25 mg/ml fibrinogen was indistinguishable from that observed in Matrigel (Suppl. Figure 1B, C). Visual comparison of successive image volumes confirmed that parasites moving through fluorescent fibrin also deform the matrix (Suppl. Figure 1D and Video 4) and undergo the striking constrictions seen in Matrigel.

To calculate and map the deformations of the fibrin matrix, we used the Fast Iterative Digital Volume Correlation (FIDVC) algorithm developed by Christian Franck's group

(https://github.com/FranckLab/FIDVC) to iteratively determine the 3D displacement fields between consecutive volumetric image stacks in our time series [33]. Each image volume is divided into 16,807 subvolumes (49 x 49 x 7 subvolumes in *x*, *y*, *z*). The algorithm compares the voxel intensity pattern between corresponding subvolumes at two consecutive timepoints, calculating one 3D displacement vector per subvolume. The data can be displayed as a map for the entire imaging volume (*e.g.*, Video 5) or for any 2D plane (*x-y*, *x-z*, or *y-z*). Most of the 2D images below show the displacement maps in the *x-y* plane on one of the seven *z* subvolume levels.

To filter out background signal and identify displacements caused by the parasite, we used timepoints when no parasites were moving to calculate a displacement detection threshold for each individual dataset (see Methods and Suppl. Figure 2A). Using this approach, the limit of detection for 3D displacement magnitudes in the system ranges from 0.042-0.046 µm; a similar 3D displacement detection threshold (0.043-0.046 µm) was observed in samples containing no parasites (Suppl. Figure 2B), validating the approach. When analyzing data in the *x-y* plane only, the background cutoff was calculated using the *x-y* displacement magnitudes (rather than the *x-y-z* displacement magnitudes); this lowered the displacement detection threshold to 0.028-0.031 µm.

In order to translate matrix displacements into the magnitude of forces generated by the parasite, we determined the viscoelasticity of the fibrin matrix using laser trapping (see Methods). The fibrin gel behaves as a predominantly elastic matrix (Suppl. Figure 3) with an elastic modulus of 15.6 pN/µm and a viscous modulus of 0.09 pN*s/µm. The minimal detectable force magnitude in this system is therefore 0.66-0.72 pN in 3D and 0.45-0.49 pN in the *x-y* plane.

**Parasite constrictions are tightly linked to periodic bursts of matrix deformation and motility**

With this system for 3D traction force mapping in hand, we analyzed the pattern and directionality of forces produced by wild-type parasites as they moved through the fibrin matrix. Plotting fibrin displacement as *x-y* maps showed that the matrix deforms in towards the parasite from all *x-y* directions at discrete, periodic time points along the trajectory, before relaxing back to its initial position (*e.g.*, Figures 2A-D and Videos 6, 7). Viewing the data as projections along each axis demonstrates that the matrix is simultaneously pulled in towards the parasite in all three dimensions (Suppl. Figure 4 and Video 5). In approximately 50% of cases, inward deformation occurred between two consecutive image volumes (1.6 seconds apart) and was followed in the next image volume by relaxation (*e.g.*, Figure 2A-C); in the remainder of cases the deformation was held through multiple time points (*e.g.*, Figure 2D) before relaxing (Suppl. Figure 5). During periods when the matrix was not being pulled inward or relaxing outward, no deformations of the matrix above background were detectable (Suppl. Figure 2A). This observation suggests either that the parasite pulls on the matrix only during some portions of its trajectory

or that the parasite produces both strong and weak deformations, and the weak deformations – which could be continuous – are below our level of detection.

When the displacement maps were overlaid onto the images of the moving parasites, it became immediately apparent that the timing of each large matrix deformation coincided with a parasite constriction and that the displacement vectors pointed primarily in towards the constriction (Figure 2C, D; additional examples are shown in Suppl. Figure 6). The fact that the displacements were directed inwards rather than away from the parasite indicates that the pinching of the parasite membrane results from pulling forces generated by the parasite rather than the parasite squeezing through a narrow pore within the matrix, which would push the matrix away. When a constriction persisted over multiple time points, the fibrin continued to deform into the constriction and/or to hold the deformation over those same time points as the parasite passed through (*e.g.*, Figure 2D).

The time it took a parasite to move completely through a constriction ranged from 1.6-56.2 seconds (average 6.8 ± 5.2 seconds, measured in brightfield) with the longer times due to a stall in forward progression of a constricting parasite. The time between one constriction finishing and another beginning was also variable (Figure 3A). In 46.3% of the cases, the end of one constriction was followed immediately by the beginning of another, while in 13.8% of the cases (n=188) a second constriction would start before the first constriction finished (Figure 3A, B and Video 8). Most importantly, all parasites that move at least one body length undergo a constriction and the total trajectory length is directly proportional to the number of constrictions observed (Figure 3C), strongly suggesting that the parasite-generated forces that create the constriction play an important role in forward movement.

The much reduced width of the parasite during a constriction (2.56 ± 0.38 µm at its widest point before constriction *vs.* 1.39 ± 0.24 µm during constriction; Figure 3D) led us to question whether the constriction presents a physical obstacle to the forward motion of the nucleus (normal nuclear diameter measured by DNA staining = 2.00 ± 0.26 µm). In parasites labeled with both a fluorescent DNA stain and a fluorescently-labeled antibody against the major surface protein, TgSAG1 (to visualize the constriction), the normally round parasite nucleus did indeed become thinner and more elongate as it passed through the constriction and regained its round shape once it was through (Figure 3E). The ratio of the nuclear dimensions perpendicular and parallel to the long axis of the parasite was 0.93 ± 0.08 in a non-constricting parasite and 0.50 ± 0.06 during a constriction. We examined whether the periodic need to squeeze the nucleus through the constriction might be responsible for the periodic changes in speed observed along the parasite's trajectory [11], but tracking analysis of constricting parasites did not reveal any consistent relationship between the instantaneous speed of the parasite and position of the nucleus relative to the constriction.

Interestingly, the distribution of the fluorescent anti-TgSAG1 antibody on the parasite surface changed as the parasite moved: much of the fluorescent signal appeared to be "swept" from anterior to posterior at the constriction as the parasite moved through (Suppl. Figure 7 and Video 9). The redistributed antibody was ultimately shed and deposited behind the moving parasite in the form of a fluorescent helical trail within the Matrigel (Suppl. Figure 7 and Video 9).

**Parasites that do not generate constrictions do not detectably deform the matrix**

Since TgMyoA is thought to play a central role in force production during parasite motility (Figure 1A), we conducted force mapping experiments using a parasite line lacking TgMyoA [17, 18]. As previously reported [25], these parasites are much less motile in 3D than wild-type parasites: only 18 of 769 TgMyoA knockout parasites examined (2.3%) moved one body length or more, compared to 99 of 278 wild-type parasites (35.6%; Suppl. Figure 8A). Of the 18 TgMyoA knockout parasites that moved at least one body length, none showed constrictions like those seen in wild-type parasites. The pattern of movement was also different from wild-type parasites; rather than moving along smooth helical trajectories, the TgMyoA knockout parasites moved in tightly twisting arcs or in a stair-like pattern consisting of right-angled turns associated with a sharp bend in the body of the parasite (Suppl. Figure 8B and Video 10). In stark contrast to the wild-type parasites, we also saw no evidence by traction force mapping of a ring of inward-directed forces produced by the TgMyoA knockouts. In fact, we did not detect any displacement of the matrix by these parasites (Suppl. Figures 2C and 8C-E), suggesting that any forces produced by the moving knockout parasites are below the limit of detection in our traction force assay.

We also tested whether the surface adhesin, TgMIC2, plays a role in generating the constriction-associated inward forces on the matrix. The motility defect in parasites lacking TgMIC2 is less severe than the defect in parasites lacking TgMyoA, with 36 of 297 TgMIC2 knockout parasites (12.1%) capable of moving more than one body length (see also [31, 34]). However, these parasites often moved in an erratic, stop and start pattern, bending sharply and moving in tightly twisting arcs (Figure 4A and Video 11). Moreover, the TgMIC2 knockout parasites also failed to form constrictions and did not detectably deform the fibrin matrix (Fig. 4A, Suppl. Figures 2D & 9C-E) despite being able to move at maximum speeds similar to wild-type parasites [31]. Taken together, these data confirm that motility is significantly altered, but not completely eliminated, in parasites lacking TgMyoA or TgMIC2. Furthermore, the data demonstrate that both proteins are required to produce the constriction and the constriction-associated inward forces on the matrix observed during the motility of wild-type parasites.

**TgMIC2-deficient parasites move less directionally**

The larger number of TgMIC2 knockout parasites capable of long runs of motility (compared to the MyoA knockouts) enabled us to analyze their phenotype in greater detail. The nuclei of the parasites lacking TgMIC2 did not change shape as they moved in 3D (Figure 4B and Suppl. Figure 9A), providing further evidence that these parasites do not undergo the constrictions seen in wild-type parasites. Given their apparent propensity for tight turns, we also quantified the ability of the TgMIC2 knockout parasites to move directionally, by comparing displacement distance to trajectory length. While parasites with and without TgMIC2 traveled along trajectories of similar mean length (38.47 ± 9.3 µm vs. 42.22 ± 8.0 µm, respectively), parasites lacking TgMIC2 moved approximately half as far from their starting point as wild-type parasites (Fig. 4C and Suppl. Figure 9B). These data suggest that the circumferential zone of attachment to the matrix, which requires TgMIC2, functions as a guidance system that converts meandering motility into more linear, directed forward progression.

## Discussion

The linear motor model of apicomplexan motility predicts that a parasite moves by pulling continuously on the matrix in an anterior-to-posterior direction along the length of the parasite. It was, therefore, unexpected that the predominant forces revealed by our new 3D traction force mapping assay were instead periodic and highly localized, pointing inwards from all directions towards a circumferential location on the parasite surface. This circular band of inward-directed force forms at a fixed position within the matrix and creates a visible constriction at the parasite periphery. The constriction passes from the anterior to the posterior end of the parasite as the parasite moves forward. Typically, when the constriction reaches the parasite's posterior end a new constriction forms at the apical end and the cycle repeats. These results suggest that the moving parasite periodically assembles ring-shaped zones of tight attachment to the matrix, which deform the matrix and serve as stationary platforms that the parasite propels itself through, one body length at a time.

**Attachment to the substrate, force generation, and motility in 2D *vs.* 3D.** Both malaria sporozoites and *T. gondii* tachyzoites are capable of moving in circles on 2D surfaces. The pioneering work of Munter, Frischknecht and colleagues combined traction force mapping with reflection interference contrast microscopy (RICM) during the 2D circular gliding of malaria sporozoites [35]. They concluded that the parasite adheres to the substrate at its apical and posterior ends; each of these adhesion sites produces stalling forces parallel to the long axis of the parasite, and disengagement of the adhesion sites drives forward motion. Traction forces perpendicular to the direction of movement were also detected at the center of the parasite but these were interpreted as nonspecific and nonproductive. The

apical and posterior adhesion sites were shown to move forward *with* the parasite, rather than remaining stationary with respect to the substrate.

*T. gondii* tachyzoites demonstrate a second form of productive motility on 2D surfaces called helical gliding: the banana-shaped parasite starts with its left side in contact with the substrate, moves forward one body length while rotating along its longitudinal axis until it lies on its right side, and then flips back to its left side to repeat the cycle [36]. This form of motility is the equivalent of the fully helical trajectories seen in 3D but constrained in 2D by contact of the curved parasite with the rigid substrate. In RICM studies of 2D helical gliding [19, 37] the tachyzoite was seen to first attach to the substrate at its apical end. The zone of attachment then expanded along the length of the parasite and, as the parasite moved forward and its apical end twisted up off the cover slip, the zone of attachment shrunk until it was reduced to a spot at the posterior end. In contrast to *Plasmodium* sporozoites, the position of the tachyzoite adhesion site remained fixed relative to the substrate and the parasite slid over this attachment site as the parasite moved forward. 2D traction force mapping revealed forces parallel, but not perpendicular, to the longitudinal axis of the tachyzoite; these traction forces, together with spring-like forces generated by the parasite's microtubule cytoskeleton, were postulated to produce forward motion [37].

When these previous studies of *T. gondii* 2D motility are combined with the 3D results presented here, a consensus emerges that the basic unit of motility consists of apical attachment to the substrate, followed by apical-to-posterior translocation of the adhesion site, which is fixed in its position relative to the substrate. When the adhesion site reaches the posterior end of the parasite, a new apical attachment site is formed, and the cycle begins again. The adhesion site in a 3D matrix is circular, and the pulling forces exerted by the parasite on the matrix manifest as a visible constriction in the parasite's plasma membrane. In 2D, no deformation of the parasite has been reported at the adhesion site, likely reflecting differences in attachment to the substrate via a point/patch on the parasite surface *vs.* circumferential attachment. We also saw no evidence in 3D for a persistent stall force at the rear of the parasite. The biggest difference between the 2D and 3D force mapping data is that, in 3D, all force vectors point towards one highly localized circumferential region on the surface of the parasite, and many of these force vectors contained a strong component perpendicular to the long axis of the parasite.

**3D motility and invasion: variations on a theme.** During the invasion of host cells by *T. gondii*, proteins secreted from the parasite's apical organelles assemble a ring-shaped zone of tight attachment between the membranes of the two cells. This "moving junction" does not in fact move: it is anchored to the host cytoskeleton and is hypothesized to provide a fixed platform against which the parasite exerts force [38-42]. Parasite surface adhesins, which are engaged with the junction via their extracellular domains, are thought to be translocated by TgMyoA in an anterior-to-posterior direction, pushing the

parasite through the junction and into the host cell. The body of the parasite narrows dramatically as it passes through the moving junction, bearing a striking resemblance to the constrictions seen during 3D motility.

Two central players in moving junction formation are TgAMA1, an adhesin secreted onto the parasite surface from the micronemes, and TgRON2, which is secreted by the parasites into the host cell plasma membrane and serves the ligand to which TgAMA1 binds. Neither TgAMA1 [43, 44] nor TgRON2 (RVS and GEW, unpublished data) plays any detectable role in parasite motility. Instead, TgMIC2 – another microneme protein secreted onto the parasite surface – likely plays an analogous role during motility to that of TgAMA1 during invasion, with TgMIC2 binding to ligands in the extracellular matrix rather than to TgRON2 in the host cell membrane.

As the parasite moves forward during both invasion and 3D motility, it simultaneously rotates around its long axis [11, 36, 45]. Our results provide a possible explanation for this rotational motion. In both cases, parasite receptors bind to their cognate ligands in the form of a circular ring of attachment that is fixed in position relative to the host cell (in the case of invasion) or the extracellular matrix (in the case of motility). It has long been proposed that the TgMyoA motor driving invasion and motility is arranged helically within the parasite, along the spiraling subcortical microtubules (*e.g.*, [37]). Alternatively, a recent modeling study suggests that the unique geometry of the parasite periphery can generate a self-organized helical pattern of anterior-to-posterior actin flow (Hueschen *et al*, submitted). In either case, if the actin filaments flow helically and are connected to the tails of transmembrane adhesins engaged circumferentially with the host cell surface or extracellular matrix, the forward motion of the parasite either into the cell or through the matrix will by definition be accompanied by rotational twist. Some portion of the perpendicular force that we observed directed towards the constriction in our traction force assays may in fact reflect torque on the matrix produced by the parasite as it twists through this circular zone of attachment.

As a parasite invades a host cell, antibodies are "shaved" off the parasite surface at the moving junction by an as yet unknown mechanism [46]. Remarkably, a similar phenomenon is observed during 3D motility: fluorescent antibody against the surface protein TgSAG1 is lost from the parasite surface anterior to the constriction and shed as a helical trail of fluorescence behind the moving parasite (Suppl. Figure 7 and Video 9).

The numerous parallels between invasion and 3D motility noted here suggest that the two processes may be more mechanistically similar than previously recognized [12, 19], with implications for our understanding of each. For example, our data suggest that 3D motility can be best described as the parasite undergoing sequential invasion-like events through circular zones of attachment to the matrix; during invasion the parasite only needs to move a single body length to penetrate into the host cell, but

during motility the parasite can string multiple constriction events together to move multiple body lengths (Figure 3C). The data also raise the possibility that the characteristic constriction of the parasite seen at the moving junction during invasion does not reflect the parasite being squeezed as it *pushes* itself through the small diameter opening into the host cell, as is commonly thought (*e.g.,* [47, 48]), but rather the parasite attaching to and *pulling* on the host cell plasma membrane as it penetrates.

**The linear motor model.** The data presented here with wild-type parasites are at least partially consistent with the linear motor model of motility, in which: (a) actin polymerization is nucleated at the apical tip of the parasite by formin1 [19]; (b) TgMyoA translocates the actin filaments in an anterior-to-posterior direction along the length of the parasite; and (c) binding of the rearward flowing actin filaments to transmembrane adhesins [14], whose extracellular domains are attached to the substrate drives the forward motion of the parasite (Figure 1A). While anterior-to-posterior actin flux may occur along the entire length of the parasite periphery (Hueschen *et al*, submitted), we propose that force is generated, at least in part, by the rearward translocation of the subset of actin filaments that are coupled to adhesins at the circular ring of attachment. We were unable to detect any anterior-to-posterior bias in the force vectors at the constriction, which would be expected if the parasite pulls against this zone of attachment in order to move forward. These forces may be below our limit of detection (~0.72 pN). Alternatively, compression of the fibrin immediately adjacent to the constriction might increase the local elastic modulus of the matrix, making it more difficult to see proximal displacements because of a local increase in the displacement detection threshold. Because the fibrin gel behaves primarily as an elastic matrix (Suppl. Figure 3), the relationship between acceleration and force is complex and we cannot calculate with any confidence how much total displacement / force would be required to achieve a given parasite velocity and relate this to the displacement detection threshold of the assay.

The marked regularity with which the parasite generates the circular zones of attachment on its surface, yielding on average one constriction per body length of motion, could be due to repetitive bursts of formin1-mediated actin polymerization at the parasite's apical tip [19] or to periodic release of adhesins such as TgMIC2 from the micronemes. Alternatively, the observation that constrictions occur back-to-back almost 50% of the time (Fig. 3A), may suggest that a new constriction forms at the apical tip before the prior constriction has ended, but this new constriction stalls as the TgMyoA (or possibly TgMyoH [19]) to which it is connected pulls against the adhesive forces of the more posterior previous constriction. Future real-time analysis of actin polymerization and microneme secretion in motile parasites and higher sensitivity force mapping will be necessary to further interrogate the periodic nature of ring assembly.

The lack of a motility-associated constriction in TgMyoA-deficient parasites could reflect an inability either to assemble ring of adhesins at the apical tip of these parasites or, more likely, to move

through the incipient ring once it has formed. Alternatively, it could be that the ring-shaped structures that form during motility are contractile, and contractility requires TgMyoA. The inward deformation of the fibrin matrix towards the constriction reported here is consistent with a contractile ring, as is the physical constriction of the parasite plasma membrane. Further experiments will be required to distinguish between these possibilities.

If the coupling of actin flow to the circular zone of attachment is important for forward motion, how do the parasites lacking TgMIC2 move at normal speeds in the absence of constrictions? It is possible that both the wild-type and mutant parasites generate small forces distributed over their entire surface (in addition to larger forces generated at the constriction in wildtype) that are collectively sufficient to drive motility but individually below our level of detection. Alternatively, the loss of TgMyoA or TgMIC2 might lead to compensatory changes in the expression of other genes with overlapping or redundant function [23, 49, 50]. The TgMIC2 KO parasites do in fact show changes in the expression of several other microneme and motility-associated proteins [31]. Perhaps most interestingly, parasites lacking TgMyoA and/or TgMIC2 might use a motility mechanism that is entirely different from that of wild-type parasites (*e.g.*, [18, 22]), does not involve a constriction, and is not as efficient as the wild-type mechanism but is nevertheless capable of supporting motility and sustaining the parasite's lytic cycle. By analogy with observations from animal cells [51], parasites might use different mechanisms for motility in different situations such as squeezing through tight junctions [8] *vs.* migrating through loose interstitial tissues. Any attempt to develop new therapeutics targeting parasite motility [52, 53] will need to take into account the possibility that the parasite has multiple mechanisms to draw upon. If the motility of the mutants is driven by a different mechanism than that of wild-type parasites, higher sensitivity 3D traction force mapping may reveal informative differences in their pattern of force generation.

**A guidance system for motility?** The forward motion of the TgMIC2 knockout parasites, which lack the circular attachment zone, is significantly more disorganized than the motility of wild-type parasites. The mutant parasites can still generate relatively long trajectories, but the trajectories take them less far from their starting point than wild-type parasites. As discussed above, attachment to the matrix via a circular ring of adhesion likely contributes to the rotational twisting of the parasite as it moves forward and thereby to the overall helicity of the parasite's trajectory. Extensive studies of the helical swimming behavior of bacteria has shown that a curved cell shape and helical trajectory are a particularly efficient way for small cells to move through viscous media [54-58]. Engagement of *T. gondii* with the extracellular matrix through a circular band of adhesion may therefore not only create a fixed platform for the parasite to pull against and move forward; it may also function as a guidance system to help the parasite move efficiently through the various environments it encounters as it disseminates through the tissues of the unfortunate organisms it infects.

## Methods

**Cell Culture.** Parasites were propagated by serial passage in human foreskin fibroblasts (HFFs). HFFs were grown to confluence in Dulbecco's Modified Eagle's Medium (DMEM) (Life Technologies, Carlsbad, CA) containing 10% (vol/vol) heat-inactivated fetal bovine serum (FBS) (Life Technologies, Carlsbad, CA), 10 mM HEPES pH 7, and 100 units/ml penicillin and 100 ug/ml streptomycin, as previously described [59]. Prior to infection with *T. gondii*, the medium was changed to DMEM supplemented with 10mM HEPES pH 7, 100 units/ml penicillin and 100 ug/ml streptomycin, and 1% (vol/vol) FBS.

**Pitta Chamber Assembly.** 22×22 coverglasses were washed with Alconox detergent, rinsed with tap water, deionized water, and ethanol (100%), and air dried. Two strips of double-sided tape (Scotch 3M, St. Paul, MN) were placed 3 mm apart on a glass slide, and the coverglass was placed on top of the tape and pressed firmly to ensure a complete seal. The flow cell volume was approximately 10 µl.

**Matrigel Matrix.** Pitta chambers containing parasites embedded in polymerized Matrigel were prepared as previously described [11]. Briefly, parasites were harvested from infected HFFs via syringe release and passed through a 3 µm Nucleopore filter (Whatman, Piscataway NJ). Parasites were pelleted and resuspended at in Live Cell Imaging Solution (LCIS) buffer. For fluorescence imaging, the LCIS contained 0.5 mg/ml Hoechst 33342 (Thermo Scientific, Waltham, MA) and/or a 1:20 dilution of Alexa546-conjugated anti-TgSAG1 (see Table 1). Fluorescent anti-TgSAG1 (100µg) was prepared using the Alexa Fluor 546 Antibody Labeling Kit (Thermo Scientific, Waltham, MA) as per the manufacturer's instructions. Parasites were incubated with the Hoechst 33342 (10 minutes) and/or anti-TgSAG1(15 minutes) at room temperature, then mixed with Matrigel and LCIS on ice in a 1:3:3 (vol/vol/vol) ratio and immediately added to a Pitta chamber. The Pitta chamber was incubated for three minutes at 35°C in a custom-build heated microscope enclosure (UVM Instrumentation and Model Facility, Burlington, VT) before imaging.

**Fibrin Matrix.** Unlabeled and Alexa-Fluor 647-labeled fibrinogen (both from Thermo Scientific, Waltham, MA) were each dissolved in 0.1M sodium bicarbonate (pH 8.3) to 15 mg/ml. Aliquots of 50 µl were flash frozen and stored at -80C until use. Fibrin gels [32] containing parasites were prepared in Pitta chambers as follows. The parasite culture medium was replaced with LCIS buffer before harvesting via

syringe release and filtering. 500 µl of the parasite suspension were pelleted and resuspended in LCIS buffer to achieve a higher parasite concentration. Parasites were mixed with fibrinogen (final fibrinogen concentration of 2.25, 4.5, or 9 mg/ml). LCIS buffer containing thrombin (Sigma, Burlington, MA) and FBS was added to the parasite-fibrinogen suspension for final concentrations of $1.5x10^8$ parasites per ml, 1 unit/ml of thrombin, and 10% FBS. The mixture was immediately pipetted into a Pitta chamber and allowed to polymerize at room temperature for three minutes before mounting on the microscope and imaging.

**Image Acquisition.** A Nikon Eclipse TE300 epifluorescence microscope (Nikon Instruments, Melville, NY) equipped with a NanoScanZ piezo Z stage insert (Prior Scientific, Rockland, MA) was used to image parasites. See Table 1 for details of the imaging setup. Time-lapse video stacks were collected with an iXON Life 888 EMCCD camera (Andor Technology, Belfast, Ireland) using NIS Elements software v.5.11 (Nikon Instruments, Melville, NY). Fluorescently labeled parasites were imaged using a pE-4000 LED illuminator (CoolLED, Andover England) and a 89402 Quad filter (Chroma, Bellows Falls, VT). Stacks consisting of individual images (1024 pixel× 384 pixel) captured 0.5-1 µm apart in *z*, covering a total of 10-40 µm, were collected using either a 20× PlanApo λ (0.65 pixel/µm, NA 0.75) or 60 × PlanApo λ (0.22 pixel/µm, NA 1.4) objective as described in Table 1. The same volume was successively imaged 60-360 times over the course of 64-302 seconds. The camera was set to trigger mode, no binning, readout speed of 35 MHz, conversion gain of 3.8x, and EM gain setting of 300.

**Table 1: Imaging parameters for the different experiments described**

| Experiment | Objective | Fluorochrome (Excitation/emission wavelengths) | Image spacing in *z* | Exposure time per image | Number of Image stacks | Total time | Volume (*x, y, z*) |
|---|---|---|---|---|---|---|---|
| Microspheres (Matrigel) | 60× | DragonGreen (490/507-530nm) | 41 slices, 1µm apart | 16 ms | 60 | 64s | 225.3 µm × 84.5 µm × 40 µm |
| | | tdTomato parasites (550/579-608 nm) | | | | | |
| Fibrin vs Matrigel and TgMIC2 KO directionality | 20× | Hoechst 33342 (385/420-449 nm) | 41 x 1 µm | 16 ms | 120 | 80s | 665.6 µm × 249.6 µm × 40 µm |
| | 60× | tdTomato parasites | 50 x 0.5 µm | 16 ms | 60 | 96s | |

| | | | | | | | |
|---|---|---|---|---|---|---|---|
| Force Mapping, WT (Fibrin) | | (550/579-608 nm)<br>Fibrin (635/666-723 nm) | | | | | 225.3 µm × 84.5 µm × 24.5 µm |
| WT, TgMyoA KO, TgMIC2 KO; Brightfield (Matrigel, fibrin) | 60× | N/A: Brightfield | 21 x 1 µm | 40 ms | 360 | 302s | 225.3 µm × 225.3 µm × 20 µm |
| Nuclear size vs constriction (Matrigel) | 20× | Hoechst 33342 (385/420-449 nm)<br>Anti-SAG1 Alexa 548 (550/579-608 nm) | 41 x 1 µm | 16 ms | 60 | 80s | 665.6 µm × 249.6 µm × 40 µm |
| TgMyoA KO Force Map (Fibrin) | 60× | Hoechst 33342 (385/420-449 nm)<br>Fibrin (635/666-723 nm) | 50 x 0.5 µm | 16 ms | 60 | 96s | 225.3 µm × 84.5 µm × 24.5 µm |
| TgMIC2 KO Force Map (Fibrin) | 60× | YFP cytosol (490/507-530 nm)<br>Fibrin (635/666-723 nm) | 50 x 0.5 µm | 16 ms | 60 | 96s | 225.3 µm × 84.5 µm × 24.5 µm |

**Tracking Parasite Motility.** Datasets were analyzed in Imaris ×64 v. 9.2.0 (Bitplane AG, Zurich, Switzerland). Fluorescently labeled parasite nuclei were tracked using the ImarisTrack module within a 1018 pixel × 380 pixel region of interest to prevent artifacts from tracking objects near the border. Spot detection used an estimated spot diameter of 3.0 × 3.0 × 6.0 µm (*x, y, z)*. A maximum distance of 6.0 µm and a maximum gap size of 2 frames were applied to the tracking algorithm. Tracks with durations under 10 seconds or displacements of less than 2 µm were discarded to avoid tracking artifacts and parasites moving by Brownian motion, respectively [11]. Accurate tracking was confirmed by visual inspection of parasite movements superimposed on their calculated trajectories.

For the comparison between Matrigel and fibrin, we analyzed three biological replicates, each consisting of three technical replicates. Student's T-tests were used to determine statistical significance between fibrin and Matrigel samples.

**Fibrin Deformation with FIDVC.** The Fast Iterative Digital Volume Correlation (FIDVC) algorithm was used to calculate 3D fibrin displacements [33] by comparing two consecutive image volumes. The image volumes were cropped to 384 × 384 pixels (*x,y)* × 48 slices (*z*) before running FIDVC. The initial interrogation window size was set to 32 × 32 × 32 and the program was run incrementally. The displacements arrows were plotted using a combination of previously described MATLAB code for 2D quiver color-coded for directionality [32] and custom MATLAB code. To filter out background signal, we calculated the mean magnitude of the 16,807 displacement vectors for each timepoint comparison in each dataset. The displacement detection threshold for that dataset was set as three standard deviations above the lowest of these mean values.

**Rheology.** A Lumicks C-Trap laser trap was used to determine the viscoelasticity of the fibrin. First, the power density spectrum (PDS) was calculated with 0.91 µm styrene beads in a flow cell. The beads were embedded in a fibrin gel, and a bead was captured in the laser trap. The flow cell was oscillated on the stage in the *y* dimension at different frequencies (1, 5, 10, 20, 50, 100 Hz), each for 5 seconds, at a fixed amplitude of 100 nm. The trap position and force in the *y* dimension were captured at 78 kHz. The elastic (in-phase) and viscous (out-of-phase) moduli were calculated using the bead's force trace. The data were analyzed in R studio. A sliding two-sided window filter, size 78, was applied to both traces. The position signal was fitted with the function $position = A * \sin(t * f - phase)$ using nonlinear least-squares with fit parameters for amplitude (A), frequency (f), and phase. The force readout was fit with the function $force = B * \sin(t * f - phase) + C * \cos(t * f - phase)$ using nonlinear least-squares with fitting parameters B and C, where B is the in-phase (elastic) component of the force. The C fit parameter divided by the velocity of the trap equals the viscous modulus.

**Confocal microscopy.** A Nikon A1R-ER point-scanning confocal microscope was used to image the fluorescent fibrin gels. Using Galvano scanning, image (1024 × 1024 pixel) stacks were captured with 60× Apo (0.1 µm/pixel, NA 1.49l) objective with 0.2 µm spacing over 5 µm. The LUNV laser was used at wavelength 633 nm and the pinhole size was 28.10 µm.

## Figure legends

**Figure 1: Parasites moving in 3D deform the surrounding Matrigel**. **(A)** In the linear motor model of motility, the TgMyoA motor (TgMyoA and its associated light chains, TgMLC1 and either TgELC1 or TgELC2) is anchored to the parasite's inner membrane complex (IMC) via the acylated protein TgGAP45 and the transmembrane proteins TgGAP40 and TgGAP50. The lumenal portion of GAP50 is thought to

interact with GAPM, a protein that spans the inner IMC membrane and likely connects the entire glideosome to the underlying parasite cytoskeleton. Short actin filaments located between the parasite plasma membrane and the IMC are connected to ligands on the substrate through a linker protein, possibly GAC, which binds to the cytosolic tails of surface adhesins such as TgMIC2. The TgMyoA motor displaces the actin filaments rearward; because the motor is connected to the IMC and the actin is connected to the substrate, this causes the parasite to move forward relative to the substrate. Modified from [26] and re-used here under the terms of a Creative Commons Attribution 4.0 International license (doi/10.1128/mSphere.00823-20). **(B)** Sequential time series images in a single *z*-plane demonstrate that Dragon Green-labeled microspheres embedded within the matrix are displaced towards moving tdTomato-expressing parasites; note displacement of the green bead closest to the fixed crosshair in the merged images. Note also constriction in the body of the fluorescent parasite in the middle two panels. See Video 1 for the entire time series, and Video 2 for a second example of bead displacement by a moving parasite. **(C)** Brightfield images showing a constriction progressing from the anterior to the posterior end of a parasite as the parasite moves forward one body length. Scale bars = 5 µm, timestamps in seconds.

**Figure 2: 3D traction force mapping in fluorescent fibrin reveals that the matrix is periodically pulled in towards the constriction during parasite motility**. **(A)** Sequential time series images in a single *z*-plane of a tdTomato-expressing parasite moving in fibrin (boxed). Scale bar = 10 µm, timestamps in seconds. **(B)** Force maps from the corresponding *z* subvolume plane of the data shown in (A); each map depicts the motions of the matrix between the two consecutive timepoints, as indicated by the brackets. Arrow length (multiplied 24-fold for display) indicates the magnitude of matrix displacement and arrow color the directionality (see color wheel). **(C)** Zoomed images showing the force maps from the boxed region of panel B, after background subtraction (see text), overlaid on the parasite images from panel A. Length of arrows indicating displacement magnitude are multiplied 15-fold for display. Note inward displacement of the matrix in the second panel, outward displacement (relaxation) of the matrix in the third panel, and no detectable displacement vectors in the fourth panel even though the parasite continues to move. See Video 6 for real-time playback of the displacement vectors overlaid on the moving parasite. **(D)** Zoomed overlays of the force maps (background subtracted) and images of a moving parasite from a second dataset. The inwardly displaced matrix in this example did not relax back to its original position within the time frame of the experiment. Arrow lengths indicating displacement magnitude are multiplied 15-fold for display. See Video 7 for real-time playback of the displacement vectors overlaid on the moving parasite. Scale bars in C and D = 5 µm. Empty red arrowheads indicate position of the constriction.

**Figure 3: The constrictions are tightly linked with motility and are sufficiently narrow to deform the parasite nucleus as it passes through. (A)** The time interval between constrictions during motility of individual parasites (n=188). A negative time interval (black bars) corresponds to the presence of two constrictions in the same parasite for the indicated amount of time. Green bars denote back-to-back constrictions and grey bars denote a delay between constrictions for the indicated amounts of time. In 27.1% of the constrictions (not plotted), no subsequent constriction occurred within the time frame of the experiment. **(B)** Example of a parasite with two concurrent constrictions. Brightfield images; scale bar = 5 µm; timestamps in seconds. **(C)** Number of constrictions observed *vs*. distance traveled, expressed in terms of binned parasite body lengths (*i.e.*, multiples of 7 µm). **(D)** Width of non-constricting parasites halfway along their longitudinal axis *vs.* width at the constriction halfway along the parasite's longitudinal axis. **(E)** Dimensions of the nucleus (as defined by Hoechst 33342 staining) in non-constricting parasites *vs*. nuclei passing through a constriction. Length is parallel and width perpendicular to the long axis of the parasite. Samples were compared by Student's two-tailed t-test.

**Figure 4: Knockout of TgMIC2 results in the loss of the constriction and less directional motility. (A)** Brightfield images showing a TgMIC2 knockout parasite moving without a constriction. Scale bar = 2.5 µm, timestamps in seconds. **(B)** Representative plots of nuclear shape (ratio of the nuclear diameter perpendicular *vs.* parallel to the long axis of the parasite) in one wildtype and one TgMIC2 knockout parasite (black circles and green squares, respectively), as the parasites moved over time. The wild-type parasite underwent multiple concurrent constrictions along its 15 µm trajectory. For the combined data from multiple parasites, see Suppl. Figure 9A. **(C)** Ratio of parasite displacement (D) to trajectory length (L) for wildtype (n= 1399) and TgMIC2 knockout (n= 165) parasites (black circles and green squares, respectively). The calculated means (± SD) are from three independent biological replicates; see Suppl. Figure 9B. In panels (B) and (C), "wildtype/WT" refers to the TgMIC2 LoxP parasites [31] before treatment with rapamycin to excise *MIC2*.

## Supplemental figure legends

**Suppl. Figure 1**: **Comparison of parasite motility in fluorescent fibrin *vs.* Matrigel. (A)** Confocal image of a 2.25 mg/ml fluorescent fibrin gel; scale bar = 10 µm. **(B)** Maximum intensity projections of tdTomato-expressing wildtype parasites moving in 3D in Matrigel (top) *vs.* fibrin (bottom). Scale bar = 40 µm. **(C)** Comparison of the maximum and mean speeds of parasites in 2.25 mg/ml fibrin *vs.* Matrigel. Horizontal bars indicate mean (± SD) from 3 independent biological replicates (Matrigel n=853, Fibrin n=913). $p > 0.05$ for both maximum and mean speed, Student's two-tailed t-test. **(D)** A parasite moving in

fluorescent fibrin (see Video 4) visibly deforms the matrix, as evident from the non-coincident fluorescence signals at two consecutive time points (merge). Scale bar = 10 µm, timestamps in seconds.

**Suppl. Figure 2**: **Determining threshold of detection in 3D traction force mapping.** The plots show all *x-y* vector magnitudes calculated by FIDVC for representative image volume datasets from **(A)** wild-type parasites, **(B)** no parasites (fluorescent fibrin only), **(C)** TgMyoA knockout parasites, and **(D)** TgMIC2 knockout parasites. Each comparison between two consecutive timepoints results in 16,807 vectors; panel A also shows an expanded plot of the 16,807 datapoints for T6-T7 (no constricting parasites in the field) and T7-T8 (one constricting parasite in the field). For each time series, the comparison between the two consecutive timepoints that gave the lowest mean displacement magnitude was used to set the background level: any displacements less than three standard deviations above this mean were considered noise for that time series.

**Suppl. Figure 3:** **Rheological properties of the fibrin matrix.** The viscoelastic properties of the fibrin matrix were measured by laser trapping of 0.91 µm styrene beads. **(A)** The laser trap position at 1 Hz (top panel) and the resulting force as measured by the laser trap (bottom) show a primarily in-phase force response. **(B)** The laser trap position and output force at 1-20Hz were used to calculate the elastic and viscous properties of the matrix; these frequencies were chosen to encompass the approximate speed of a moving parasite. Bars indicate mean (± SD).

**Suppl. Figure 4**: **All displacement vectors point in towards a moving parasite**. Matrix displacement vectors from all subvolumes (49 (*x)* x 49 (*y*) X 7 (*z*)) in the image volume were calculated by FIDVC and projected onto the *x-y, x-z* and *y-z* planes, as indicated (axis labels are in µm). Length of arrows indicate displacement magnitude and are multiplied 10-fold for display. The data correspond to the parasite shown in the second panel of Figure 2C and frame 2 of video 6. The moving parasite is outlined on each z slice with red circles, and the position of the constriction is indicated by either an empty arrowhead (*x-y*) or a black dot (*y-z*).

**Suppl. Figure 5**: **Pattern of pulling, holding and release of the matrix during individual constriction events.** The number of consecutive frames in which: the matrix displaced in towards the parasite (pull); no further matrix displacement was observed (hold); and the matrix moved away from the parasite towards its original position (release) are indicated. Total number of constrictions analyzed = 25.

**Suppl. Figure 6**: **Additional examples showing that matrix displacement is directed primarily in towards the constriction in moving parasites.** Empty red arrowheads indicate position of the constriction and white arrows the direction of parasite travel. Length of black arrows indicating displacement magnitude are multiplied 15-fold for display. Scale bars = 5 µm.

**<u>Suppl. Figure 7</u>: Fluorescent antibody against TgSAG1 is depleted from the parasite surface anterior to the constriction and shed into the matrix.** The top panels show the anti-TgSAG1 fluorescent signal; red empty arrowhead marks the location of the constriction. Middle panels show the Hoechst 33342-stained nucleus, which stays in focus throughout the time series. Bottom panels show the merged images (red = anti-TgSAG1, blue = H33342). Scale bar = 5 µm; timestamps in seconds. See Video 9 for real0time playback of the entire time series.

**<u>Suppl. Figure 8</u>: The small number of TgMyoA knockout parasites that move more than one body length show no evidence of constrictions and produce no detectable force on the fibrin matrix. (A)** Far fewer TgMyoA knockout parasites move more than one body length compared to wild-type parasites (*i.e.,* LoxP TgMyoA parasites before rapamycin treatment). **(B)** Brightfield images of a right-angled "stairstep" turn made by a moving TgMyoA knockout parasite. Scale bars = 5 µm, timestamps in seconds. **(C-E)** Sequential fluorescence images in a single *z*-plane of a moving TgMyoA knockout parasite stained with Hoechst 33342 (to label the parasite nucleus), the corresponding force maps, and the zoomed images (panel E) showing the force maps from panel D (boxed region), with background subtraction, overlaid on the parasite images from panel C. The highlighted parasite continued to move for another 24 sec; no signal above background was seen on the force maps at any time along its trajectory. Length of arrows indicating displacement magnitude are multiplied 24-fold in (C) and 15-fold in (D) for display. Scale bar = 5 µm, timestamps in seconds.

**<u>Suppl. Figure 9</u>: TgMIC2 knockout parasites show no evidence of constrictions, produce no detectable force on the fibrin matrix and move less directionally. (A)** Ratio of nuclear diameter perpendicular (width) *vs.* parallel (length) to the long axis of the parasite in moving wild-type (n=9) and TgMIC2 knockout (n=10) parasites over time. The lower width/length ratios (~0.5) seen in wild-type parasites correspond to time points during which the nuclei were squeezing through a constriction. **(B)** Ratio of parasite displacement to trajectory length for wild-type and TgMIC2 knockout parasites (three biological replicates, each consisting of three technical replicates). The horizontal bars indicate means (+/- SD), which were compared by Student's two-sided t-test. Note that in panels A and B, "wildtype/WT" refers to the TgMIC2 LoxP parasites [31] before treatment with rapamycin to excise *MIC2*. **(C-E)** Sequential fluorescence images in a single *z*-plane of a moving TgMIC2 knockout parasite expressing YFP, the corresponding force maps, and the zoomed images (panel E) showing the force maps from panel D (boxed region), with background subtraction, overlaid on the parasite images from panel C. The highlighted parasite continued to move for another 18 sec; no signal above background was seen on the force maps at any time along its trajectory. Length of arrows indicating displacement magnitude are

multiplied 24-fold in (C) and 15-fold in (D) for display. Scale bars = 10 µm (panel C), 5 µm (panel E); timestamps in seconds.

**Videos**

**Video 1:** Microsphere (green) being displaced towards a parasite (red) moving in Matrigel within in a single *z* plane. Playback is in real time; scale bar = 5 µm. Single frames from this video are shown in Figure 1B.

**Video 2:** Maximum intensity projection in *z* of microspheres (green) being displaced due to parasite (red) movement within the Matrigel. Playback is in real time; scale bar = 5 µm.

**Video 3:** Brightfield imaging of a parasite undergoing a single constriction. Playback is in real time; scale bar = 5 µm. Single frames from this video are shown in Figure 1C.

**Video 4:** Deformation of fluorescent fibrin (green) by a parasite (red; bottom) as it moves up through the image stack. Playback is in real time; scale bar = 10 µm. Single frames from this video are shown in Suppl. Figure 1D.

**Video 5:** 3D displacement map surrounding the moving parasite shown in the second panel of Figure 2C and frame 2 of Video 6. Length of arrows indicating displacement magnitude are multiplied 10-fold for display. The parasite is outlined on each z plane with red circles. Single frames from this video displaying projections onto the *x-y, x-z* and *y-z* planes are shown in Suppl. Figure 4.

**Video 6:** *x-y* displacement map overlaid on the moving parasite shown in Figure 2A-C. Playback is in real time. Arrow size corresponds to relative displacement magnitude and arrow color to displacement direction as described in Figure 2.

**Video 7:** *x-y* displacement map overlaid on the moving parasite shown in Figure 2D. Playback is in real time. Arrow size corresponds to relative displacement magnitude and arrow color to displacement direction as described in Figure 2.

**Video 8:** Brightfield imaging of a parasite undergoing two constrictions at the same time. Playback is in real time; scale bar = 5 µm. Single frames from this video are shown in Figure 3B.

**Video 9:** Parasite labeled with Alexa546-conjugated anti-TgSAG1 (red) and Hoechst 33342 (blue) undergoing a constriction. Playback is in real time; scale bar = 5 µm. Note the helical trail of shed fluorescent antibody behind the moving parasite. Single frames from this video are shown in Suppl. Figure 7.

**Video 10:** Brightfield imaging of a moving TgMyoA knockout parasite. Playback is in real time; scale bar = 5 µm. Single frames from this video are shown in Suppl. Figure 8B.

**Video 11:** Brightfield imaging of a moving TgMIC2 knockout parasite. Playback is in real time; scale bar = 5 µm. Single frames from this video are shown in Figure 4A.

**Acknowledgements.** This work was supported by U.S. Public Health Service grants: AI139201 and AI137767 (G.E.W): GM141743 and S10OD026884 for the Lumicks C-Trap (D.M.W); and T32AI055402 and F31AI145214 (R.V.S.), as well as American Heart Association grant 19PRE34370071 (R.V.S.) We thank Nicole Bouffard and Dr. Douglas Taatjes of the UVM Larner College of Medicine Microscopy Imaging Center (RRID# SCR_018821) for helpful advice and assistance with the Nikon A1R-ER confocal microscope, which is supported by U.S. Public Health Service grant 1S10OD025030-01 from the National Center for Research Resources. We thank: Dr. Markus Meissner for sharing the TgMyoA and TgMIC2 knockout parasites; Dr. David Sibley for anti-TgSAG1 antibody; Drs. Mark Rould, Alex Dunn, Christina Hueschen, Li-av Segev Zarko, John Boothroyd, Leanna Owen, Markus Meissner, and Ulrich Schwarz for helpful discussions; Anne Snyder, Drs. Robyn Kent, Christina Hueschen, and Chris Huston for helpful feedback on the manuscript. Finally, we thank Dr. Christian Franck for making the FIDVC code used in this work freely available through GitHub.

## References

1. Bigna JJ, Tochie JN, Tounouga DN, Bekolo AO, Ymele NS, Youda EL, et al. Global, regional, and country seroprevalence of Toxoplasma gondii in pregnant women: a systematic review, modelling and meta-analysis. Sci Rep. 2020;10(1):12102. Epub 2020/07/23. doi: 10.1038/s41598-020-69078-9. PubMed PMID: 32694844; PubMed Central PMCID: PMCPMC7374101.
2. Flegr J, Prandota J, Sovičková M, Israili ZH. Toxoplasmosis--a global threat. Correlation of latent toxoplasmosis with specific disease burden in a set of 88 countries. PLOS One. 2014;9(3):e90203. Epub 2014/03/26. doi: 10.1371/journal.pone.0090203. PubMed PMID: 24662942; PubMed Central PMCID: PMCPMC3963851.
3. Pappas G, Roussos N, Falagas ME. Toxoplasmosis snapshots: global status of *Toxoplasma gondii* seroprevalence and implications for pregnancy and congenital toxoplasmosis. Int J Parasitol. 2009;39(12):1385-94. Epub 2009/05/13. doi: 10.1016/j.ijpara.2009.04.003. PubMed PMID: 19433092.
4. Rothova A. Ocular involvement in toxoplasmosis. British Journal of Ophthalmology. 1993;77(6):371-7. doi: doi: 10.1136/bjo.77.6.371.
5. Su E, Honda A, Latkany P. Ocular Disease due to *Toxoplasma gondii*. In: Weiss LM, Kim K, editors. *Toxoplasma gondii* - The Model Apicomplexan: Perspectives and Methods. Second ed. London, UK: Academic Press; 2014. p. 161-92.
6. Daher W, Plattner F, Carlier MF, Soldati-Favre D. Concerted action of two formins in gliding motility and host cell invasion by *Toxoplasma gondii*. PLOS Pathog. 2010;6(10). PubMed PMID: 20949068.

7. Elsheikha HM, Marra CM, Zhu XQ. Epidemiology, Pathophysiology, Diagnosis, and Management of Cerebral Toxoplasmosis. Clinical microbiology reviews. 2021;34(1). Epub 2020/11/27. doi: 10.1128/cmr.00115-19. PubMed PMID: 33239310.

8. Barragan A, Brossier F, Sibley LD. Transepithelial migration of *Toxoplasma gondii* involves an interaction of intercellular adhesion molecule 1 (ICAM-1) with the parasite adhesin MIC2. Cell Microbiol. 2005;7(4):561-8. PubMed PMID: 15760456.

9. Harker KS, Ueno N, Lodoen MB. *Toxoplasma gondii* Dissemination: A Parasite's Journey through the Infected Host. Parasite Immunol. 2015;37:141-9. Epub 2014/11/20. doi: 10.1111/pim.12163. PubMed PMID: 25408224.

10. Meissner M, Schluter D, Soldati D. Role of *Toxoplasma gondii* myosin A in powering parasite gliding and host cell invasion. Science. 2002;298(5594):837-40. PubMed PMID: 12399593.

11. Leung JM, Rould MA, Konradt C, Hunter CA, Ward GE. Disruption of *TgPHIL1* alters specific parameters of *Toxoplasma gondii* motility measured in a quantitative, three-dimensional live motility assay. PLOS One. 2014;9(1):e85763. Epub 2014/02/04. doi: 10.1371/journal.pone.0085763. PubMed PMID: 24489670; PubMed Central PMCID: PMC3906025.

12. Frenal K, Dubremetz JF, Lebrun M, Soldati-Favre D. Gliding motility powers invasion and egress in Apicomplexa. Nat Rev Microbiol. 2017;15(11):645-60. doi: 10.1038/nrmicro.2017.86. PubMed PMID: 28867819.

13. Heintzelman MB. Gliding motility in apicomplexan parasites. Semin Cell Dev Biol. 2015. Epub 2015/10/03. doi: 10.1016/j.semcdb.2015.09.020. PubMed PMID: 26428297.

14. Jacot D, Tosetti N, Pires I, Stock J, Graindorge A, Hung YF, et al. An Apicomplexan Actin-Binding Protein Serves as a Connector and Lipid Sensor to Coordinate Motility and Invasion. Cell Host Microbe. 2016;20(6):731-43. doi: 10.1016/j.chom.2016.10.020. PubMed PMID: 27978434.

15. Sibley LD. Intracellular parasite invasion strategies. Science. 2004;304(5668):248-53. PubMed PMID: 15073368.

16. Kappe S, Bruderer T, Gantt S, Fujioka H, Nussenzweig V, Menard R. Conservation of a gliding motility and cell invasion machinery in apicomplexan parasites. J Cell Biol. 1999;147(5):937-44.

17. Andenmatten N, Egarter S, Jackson AJ, Jullien N, Herman JP, Meissner M. Conditional genome engineering in *Toxoplasma gondii* uncovers alternative invasion mechanisms. Nat Methods. 2012;10(2):125-7. Epub 2012/12/25. doi: 10.1038/nmeth.2301. PubMed PMID: 23263690; PubMed Central PMCID: PMC3605914.

18. Egarter S, Andenmatten N, Jackson AJ, Whitelaw JA, Pall G, Black JA, et al. The *Toxoplasma* Acto-MyoA motor complex is important but not essential for gliding motility and host cell invasion. PLOS One. 2014;9(3):e91819. Epub 2014/03/19. doi: 10.1371/journal.pone.0091819. PubMed PMID: 24632839; PubMed Central PMCID: PMC3954763.

19. Tosetti N, Dos Santos Pacheco N, Soldati-Favre D, Jacot D. Three F-actin assembly centers regulate organelle inheritance, cell-cell communication and motility in Toxoplasma gondii. eLife. 2019;8. Epub 2019/02/13. doi: 10.7554/eLife.42669. PubMed PMID: 30753127; PubMed Central PMCID: PMCPMC6372287.

20. Dobrowolski JM, Sibley LD. *Toxoplasma* invasion of mammalian cells is powered by the actin cytoskeleton of the parasite. Cell. 1996;84(6):933-9.

21. Frenal K, Polonais V, Marq JB, Stratmann R, Limenitakis J, Soldati-Favre D. Functional dissection of the apicomplexan glideosome molecular architecture. Cell Host Microbe. 2010;8(4):343-57. PubMed PMID: 20951968.

22. Gras S, Jimenez-Ruiz E, Klinger CM, Schneider K, Klingl A, Lemgruber L, et al. An endocytic-secretory cycle participates in Toxoplasma gondii in motility. PLOS Biol. 2019;17(6):e3000060. Epub 2019/06/25. doi: 10.1371/journal.pbio.3000060. PubMed PMID: 31233488.

23. Meissner M, Ferguson DJ, Frischknecht F. Invasion factors of apicomplexan parasites: essential or redundant? Curr Opin Microbiol. 2013;16(4):438-44. Epub 2013/06/04. doi: 10.1016/j.mib.2013.05.002. PubMed PMID: 23727286.

24. Tardieux I, Baum J. Reassessing the mechanics of parasite motility and host-cell invasion. J Cell Biol. 2016;214(5):507-15. doi: 10.1083/jcb.201605100. PubMed PMID: 27573462; PubMed Central PMCID: PMCPMC5004448.

25. Whitelaw JA, Latorre-Barragan F, Gras S, Pall GS, Leung JM, Heaslip A, et al. Surface attachment, promoted by the actomyosin system of *Toxoplasma gondii* is important for efficient gliding motility and invasion. BMC biology. 2017;15(1):1. doi: 10.1186/s12915-016-0343-5. PubMed PMID: 28100223; PubMed Central PMCID: PMCPMC5242020.

26. Rompikuntal PK, Kent RS, Foe IT, Deng B, Bogyo M, Ward GE. Blocking Palmitoylation of Toxoplasma gondii Myosin Light Chain 1 Disrupts Glideosome Composition but Has Little Impact on Parasite Motility. mSphere. 2021;6(3). Epub 2021/05/21. doi: 10.1128/mSphere.00823-20. PubMed PMID: 34011689.

27. Carey KL, Westwood NJ, Mitchison TJ, Ward GE. A small-molecule approach to studying invasive mechanisms of *Toxoplasma gondii*. Proc Natl Acad Sci U S A. 2004;101(19):7433-8. doi: 10.1073/pnas.0307769101. PubMed PMID: 15123807.

28. Mehta S, Sibley LD. *Toxoplasma gondii* actin depolymerizing factor acts primarily to sequester G-actin. J Biol Chem. 2010;285(9):6835-47. PubMed PMID: 20042603.

29. Wetzel DM, Hakansson S, Hu K, Roos D, Sibley LD. Actin filament polymerization regulates gliding motility by apicomplexan parasites. Mol Biol Cell. 2003;14(2):396-406. PubMed PMID: 12589042.

30. Farrell A, Thirugnanam S, Lorestani A, Dvorin JD, Eidell KP, Ferguson DJ, et al. A DOC2 protein identified by mutational profiling is essential for apicomplexan parasite exocytosis. Science. 2012;335(6065):218-21. Epub 2012/01/17. doi: 10.1126/science.1210829. PubMed PMID: 22246776; PubMed Central PMCID: PMCPMC3354045.

31. Gras S, Jackson A, Woods S, Pall G, Whitelaw J, Leung JM, et al. Parasites lacking the micronemal protein MIC2 are deficient in surface attachment and host cell egress, but remain virulent *in vivo* [version 1]. Wellcome Open Research. 2017;2:32. doi: 10.12688/wellcomeopenres.11594.1.

32. Owen LM, Adhikari AS, Patel M, Grimmer P, Leijnse N, Kim MC, et al. A cytoskeletal clutch mediates cellular force transmission in a soft, three-dimensional extracellular matrix. Mol Biol Cell. 2017;28(14):1959-74. Epub 2017/06/09. doi: 10.1091/mbc.E17-02-0102. PubMed PMID: 28592635; PubMed Central PMCID: PMCPMC5541846.

33. Bar-Kochba E, Toyjanova J, Andrews E, Kim K-S, Franck C. A Fast Iterative Digital Volume Correlation Algorithm for Large Deformations. Experimental Mechanics2015. p. 261-74.

34. Huynh MH, Carruthers VB. *Toxoplasma* MIC2 is a major determinant of invasion and virulence. PLOS Pathog. 2006;2(8):e84. PubMed PMID: 16933991.

35. Munter S, Sabass B, Selhuber-Unkel C, Kudryashev M, Hegge S, Engel U, et al. *Plasmodium* sporozoite motility is modulated by the turnover of discrete adhesion sites. Cell Host Microbe. 2009;6(6):551-62. PubMed PMID: 20006843.

36. Hakansson S, Morisaki H, Heuser J, Sibley LD. Time-lapse video microscopy of gliding motility in *Toxoplasma gondii* reveals a novel, biphasic mechanism of cell locomotion. Mol Biol Cell. 1999;10(11):3539-47.

37. Pavlou G, Touquet B, Vigetti L, Renesto P, Bougdour A, Debarre D, et al. Coupling Polar Adhesion with Traction, Spring and Torque Forces Allows High Speed Helical Migration of the Protozoan Parasite Toxoplasma. ACS nano. 2020;14:7121-39. Epub 2020/05/21. doi: 10.1021/acsnano.0c01893. PubMed PMID: 32432851.

38. Alexander DL, Mital J, Ward GE, Bradley P, Boothroyd JC. Identification of the moving junction complex of *Toxoplasma gondii*: a collaboration between distinct secretory organelles. PLOS Pathog. 2005;1(2):e17. doi: 10.1371/journal.ppat.0010017. PubMed PMID: 16244709.

39. Besteiro S, Dubremetz JF, Lebrun M. The moving junction of apicomplexan parasites: a key structure for invasion. Cell Microbiol. 2011;13(6):797-805. PubMed PMID: 21535344.

40. Dubremetz JF. Host cell invasion by *Toxoplasma gondii* [see comments]. Trends Microbiol. 1998;6(1):27-30.

41. Lebrun M, Michelin A, El Hajj H, Poncet J, Bradley PJ, Vial H, et al. The rhoptry neck protein RON4 re-localizes at the moving junction during *Toxoplasma gondii* invasion. Cell Microbiol. 2005;7(12):1823-33. PubMed PMID: 16309467.

42. Porchet-Hennere E, Torpier, G. [Relationships between *Toxoplasma* and its host cell]. Protistologica. 1983;19:357-70.

43. Bargieri DY, Andenmatten N, Lagal V, Thiberge S, Whitelaw JA, Tardieux I, et al. Apical membrane antigen 1 mediates apicomplexan parasite attachment but is dispensable for host cell invasion. Nat Commun. 2013;4:2552. Epub 2013/10/11. doi: 10.1038/ncomms3552. PubMed PMID: 24108241.

44. Mital J, Meissner M, Soldati D, Ward GE. Conditional expression of *Toxoplasma gondii* apical membrane antigen-1 (TgAMA1) demonstrates that TgAMA1 plays a critical role in host cell invasion. Mol Biol Cell. 2005;16(9):4341-9. doi: 10.1091/mbc.E05-04-0281. PubMed PMID: 16000372.

45. Pavlou G, Biesaga M, Touquet B, Lagal V, Balland M, Dufour A, et al. Toxoplasma Parasite Twisting Motion Mechanically Induces Host Cell Membrane Fission to Complete Invasion within a Protective Vacuole. Cell Host Microbe. 2018;24(1):81-96.e5. Epub 2018/07/17. doi: 10.1016/j.chom.2018.06.003. PubMed PMID: 30008293.

46. Dubremetz JF, Rodriguez C, Ferreira E. *Toxoplasma gondii*: redistribution of monoclonal antibodies on tachyzoites during host cell invasion. Exp Parasitol. 1985;59(1):24-32.

47. Herm-Gotz A, Weiss S, Stratmann R, Fujita-Becker S, Ruff C, Meyhofer E, et al. *Toxoplasma gondii* myosin A and its light chain: a fast, single-headed, plus-end-directed motor. EMBO J. 2002;21(9):2149-58.

48. Mordue DG, Desai N, Dustin M, Sibley LD. Invasion by *Toxoplasma gondii* Establishes a Moving Junction That Selectively Excludes Host Cell Plasma Membrane Proteins on the Basis of Their Membrane Anchoring. J Exp Med. 1999;190(12):1783-92.

49. Frenal K, Soldati-Favre D. Plasticity and Redundancy in Proteins Important for *Toxoplasma* Invasion. PLOS Pathog. 2015;11(8):e1005069. Epub 2015/08/14. doi: 10.1371/journal.ppat.1005069. PubMed PMID: 26270966; PubMed Central PMCID: PMC4536160.

50. Lamarque MH, Roques M, Kong-Hap M, Tonkin ML, Rugarabamu G, Marq JB, et al. Plasticity and redundancy among AMA-RON pairs ensure host cell entry of *Toxoplasma* parasites. Nat Commun. 2014;5:4098. Epub 2014/06/18. doi: 10.1038/ncomms5098. PubMed PMID: 24934579.

51. Lammermann T, Bader BL, Monkley SJ, Worbs T, Wedlich-Soldner R, Hirsch K, et al. Rapid leukocyte migration by integrin-independent flowing and squeezing. Nature. 2008;453(7191):51-5. doi: 10.1038/nature06887. PubMed PMID: 18451854.

52. Powell CJ, Ramaswamy R, Kelsen A, Hamelin DJ, Warshaw DM, Bosch J, et al. Structural and mechanistic insights into the function of the unconventional class XIV myosin MyoA from Toxoplasma gondii. Proc Natl Acad Sci U S A. 2018;115(45):E10548-e55. Epub 2018/10/24. doi: 10.1073/pnas.1811167115. PubMed PMID: 30348763; PubMed Central PMCID: PMCPMC6233092.

53. Trivedi DV, Nag S, Spudich A, Ruppel KM, Spudich JA. The Myosin Family of Mechanoenzymes: From Mechanisms to Therapeutic Approaches. Annu Rev Biochem. 2020;89:667-93. Epub 2020/03/15. doi: 10.1146/annurev-biochem-011520-105234. PubMed PMID: 32169021.

54. Berg HC, Turner L. Movement of microorganisms in viscous environments. Nature. 1979;278(5702):349-51. Epub 1979/03/22. doi: 10.1038/278349a0. PubMed PMID: 370610.

55. Ferrero RL, Lee A. Motility of Campylobacter jejuni in a viscous environment: comparison with conventional rod-shaped bacteria. Journal of general microbiology. 1988;134(1):53-9. Epub 1988/01/01. doi: 10.1099/00221287-134-1-53. PubMed PMID: 3053972.

56. Hazell SL, Lee A, Brady L, Hennessy W. Campylobacter pyloridis and gastritis: association with intercellular spaces and adaptation to an environment of mucus as important factors in colonization of the gastric epithelium. J Infect Dis. 1986;153(4):658-63. Epub 1986/04/01. doi: 10.1093/infdis/153.4.658. PubMed PMID: 3950447.

57. Kaiser GE, Doetsch RN. Letter: Enhanced translational motion of Leptospira in viscous environments. Nature. 1975;255(5510):656-7. Epub 1975/06/19. doi: 10.1038/255656a0. PubMed PMID: 1134561.

58. Kimsey RB, Spielman A. Motility of Lyme disease spirochetes in fluids as viscous as the extracellular matrix. J Infect Dis. 1990;162(5):1205-8. Epub 1990/11/01. doi: 10.1093/infdis/162.5.1205. PubMed PMID: 2230247.

59. Roos DS, Donald RG, Morrissette NS, Moulton AL. Molecular tools for genetic dissection of the protozoan parasite *Toxoplasma gondii*. Methods in Cell Biology. 451994. p. 27-63.

Figure 1

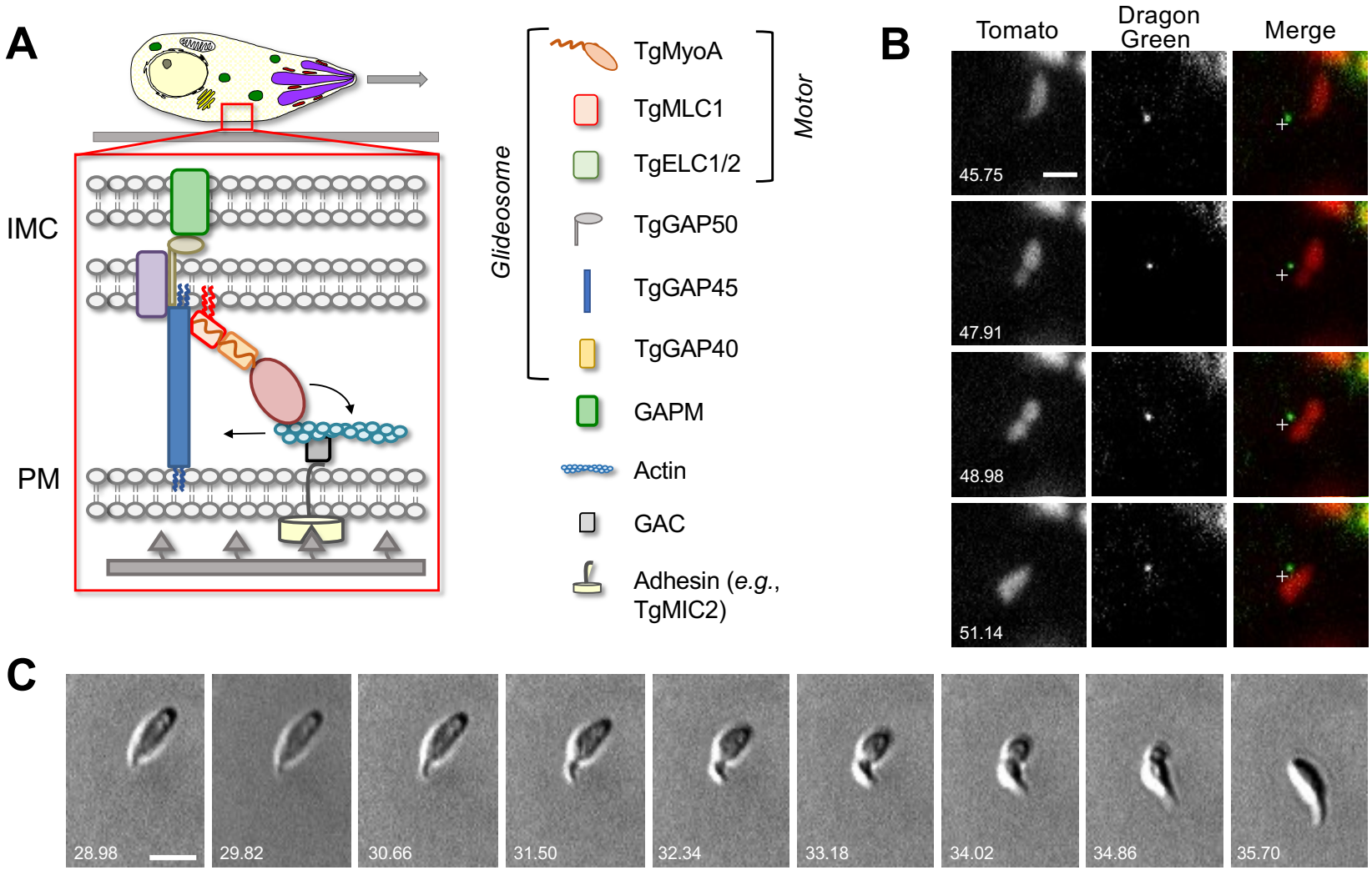
A
IMC
PM
Glideosome
Motor
TgMyoA
TgMLC1
TgELC1/2
TgGAP50
TgGAP45
TgGAP40
GAPM
Actin
GAC
Adhesin (e.g., TgMIC2)
B
Tomato
Dragon Green
Merge
45.75
47.91
48.98
51.14
C
28.98
29.82
30.66
31.50
32.34
33.18
34.02
34.86
35.70

Figure 2

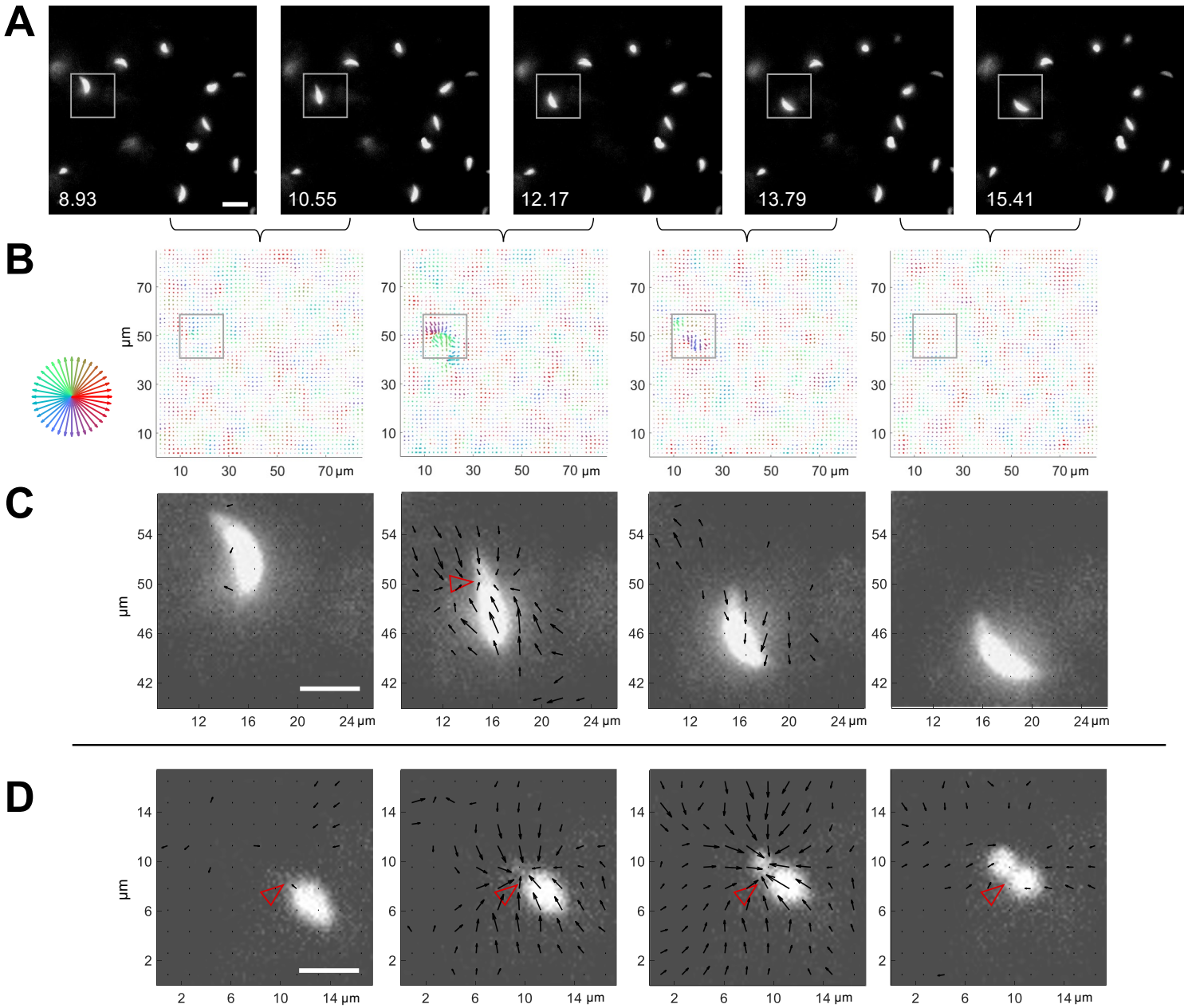

Figure 3

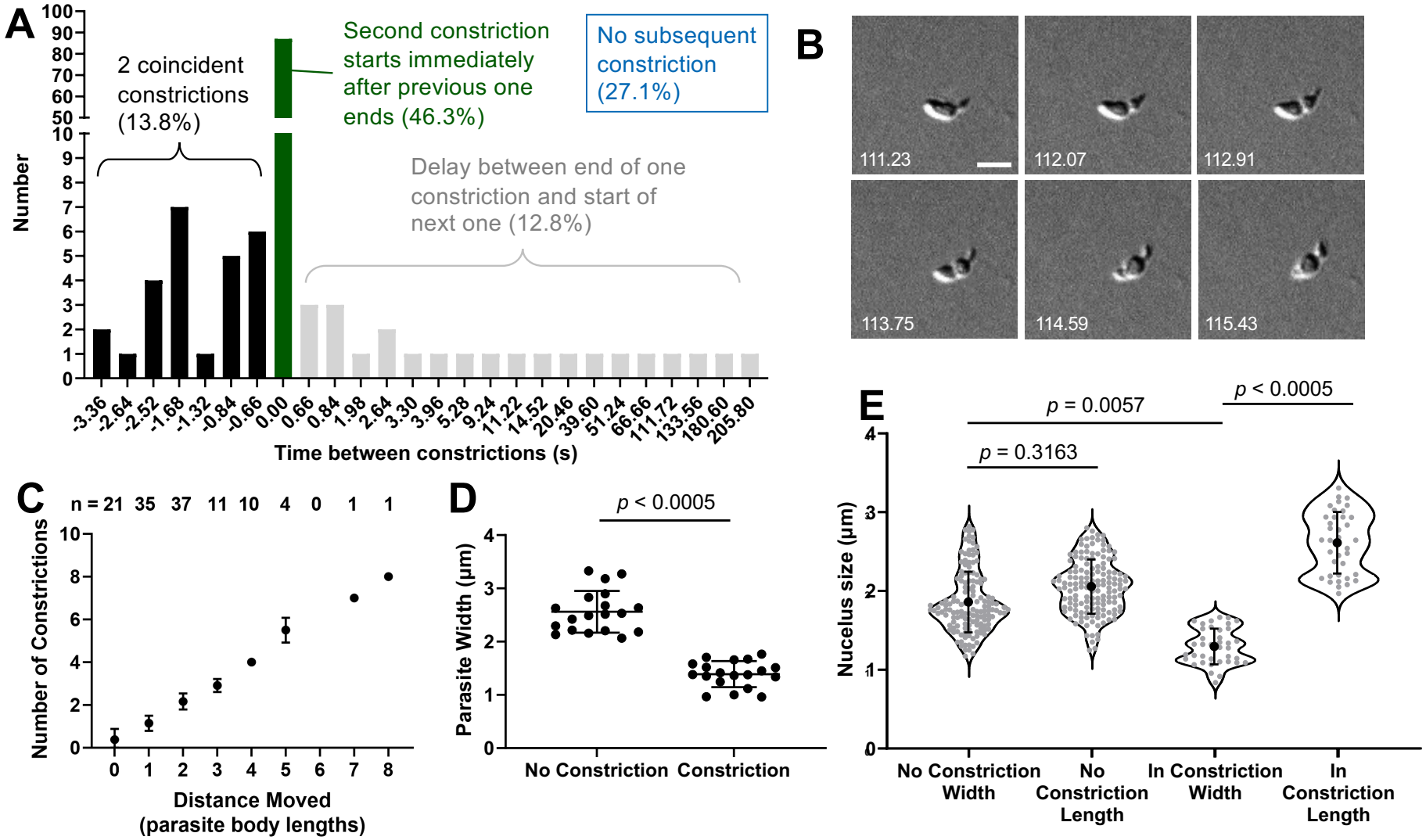
A
2 coincident constrictions (13.8%)
Second constriction starts immediately after previous one ends (46.3%)
No subsequent constriction (27.1%)
Delay between end of one constriction and start of next one (12.8%)
Number
Time between constrictions (s)
B
111.23
112.07
112.91
113.75
114.59
115.43
C
n = 21 35 37 11 10 4 0 1 1
Number of Constrictions
Distance Moved (parasite body lengths)
D
p < 0.0005
Parasite Width (µm)
No Constriction
Constriction
E
p = 0.0057
p < 0.0005
p = 0.3163
Nucelus size (µm)
No Constriction Width
No Constriction Length
In Constriction Width
In Constriction Length

Figure 4

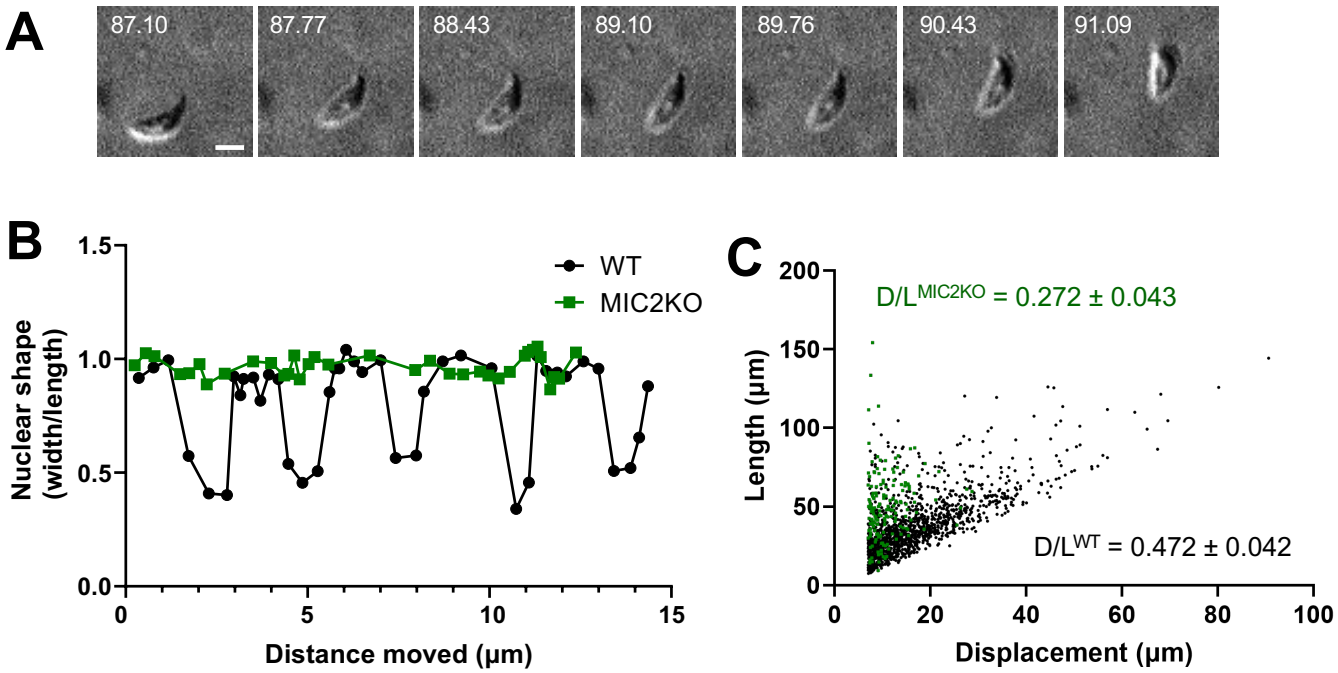
A
87.10
87.77
88.43
89.10
89.76
90.43
91.09
B
WT
MIC2KO
Nuclear shape (width/length)
1.5
1.0
0.5
0.0
0
5
10
15
Distance moved (μm)
C
D/L^MIC2KO = 0.272 ± 0.043
D/L^WT = 0.472 ± 0.042
Length (μm)
200
150
100
50
0
0
20
40
60
80
100
Displacement (μm)